Proceedings of ASME Turbo Expo 2011
GT2011
June 6-10, 2011, Vancouver, British Columbia, Canada

GT2011-45424

ROUGHNESS MODELING FOR TURBOMACHINERY

Andreas Fiala*
MTU Aero Engines GmbH
Dachauer Str. 665,
D - 80995 Munich, Germany
Email: Andreas.Fiala@mtu.de

Edmund Kügeler
Institute of Propulsion Technology
German Aerospace Center (DLR)
Linder Höhe, D - 51147 Cologne, Germany
Email: Edmund.Kuegeler@dlr.de

ABSTRACT

Fundamental concepts for roughness modeling have been further explored and advanced. A basic understanding of the effect of distributed roughness on fully developed turbulent boundary layer, its possible influence on transition, and the mechanism of local spanwise roughness on transition has been achieved. Predictions with a refinement around a spanwise roughness element have been conducted in comparison to TATMo's turbine cascade investigated at VKI. 3d-computations document the status in comparison to the T106C measurements with spanwise roughness for all Reynolds-numbers with two different transition models. Additional validation work shows the reproduction of accurate behavior of influence of height, location, and shape of the roughness element on pitchwise averaged loss and exit angle at midspan. Beside the correct reproduction of flow quantities for the spanwise roughness element, the right assessment of distributed roughness on surfaces of an industrial configuration is important. Because a high grid resolution very near the wall on all surfaces is not always possible, the problem can be solved with the help of wall-functions. The results of the application document the significance of rough wall-function modeling for tubomachinery.

INTRODUCTION

Surfaces on turbomachinery blades often show distributed roughness. The roughness stems from machining processes, from manufacturing imperfections, and the blades are subjected to erosion by impinging of particles from the combustion process in the course of their lifetimes. Surface roughness can have a profound effect on losses and on heat transfer. For a review the reader is directed to Bons [1] and the contextual sequence of the reference list. It will be shown in the following that the layer very near the surface, the viscous sublayer, loses its ability for dissipation of turbulent motions. In parallel, the height of this layer is lowered for the intermediate or transitional-rough wall. For further increased roughness, for fully rough walls, the height of the sublayer again recovers but at the expense of increased production of turbulent motions. It becomes clear that momentum exchange and that heat transfer rates are dramatically affected by this.

The enhanced momentum exchange also plays an important role for the singular spanwise roughness element. The element is at the moment an application candidate for the rear-loaded design of the last blade rows in a Low Pressure Turbine at very low Reynolds-number and most effective for the High-lift design. The effect of enhanced exchange is locally restricted to the region downstream of the single roughness element. The amplification of disturbances in the approaching laminar boundary layer is thereby increased by the element or at least, significant disturbances are introduced. This helps a separation bubble evident at very low Reynolds-number to reattach well before the trailing edge, so that no minder-deviation of the blade‟s flow angle occurs. If the roughness element is placed downstream of transition in the fully developed turbulent boundary layer, the physics is the same as the flow of distributed roughness with enlarged distance between the elements. This, we will recognize in the following roughness classification in more detail.

Roughness classification

Roughness is classified by its height and its structure. While the parameter "height" is a straightforward defined quantity, the "structure" needs some more explanation, especially with respect to its effect on the underlying flow. The examination of the structure of the model roughness of hemispheres can be helpful. Here, the most important structure parameter is the distance between the roughness elements s_0 normalized by the roughness height R_z (others, but less significant higher order parameters are described by Waigh et al. [5]).

The underlying flow is at first order characterized by the roughness structure parameter s_0/R_z. Moreover, the easy to

* Address all correspondence to this author.

determine parameter R_a /R_z is a unique function of s_0 /R_z. The relation is shown in **Figure 1**.

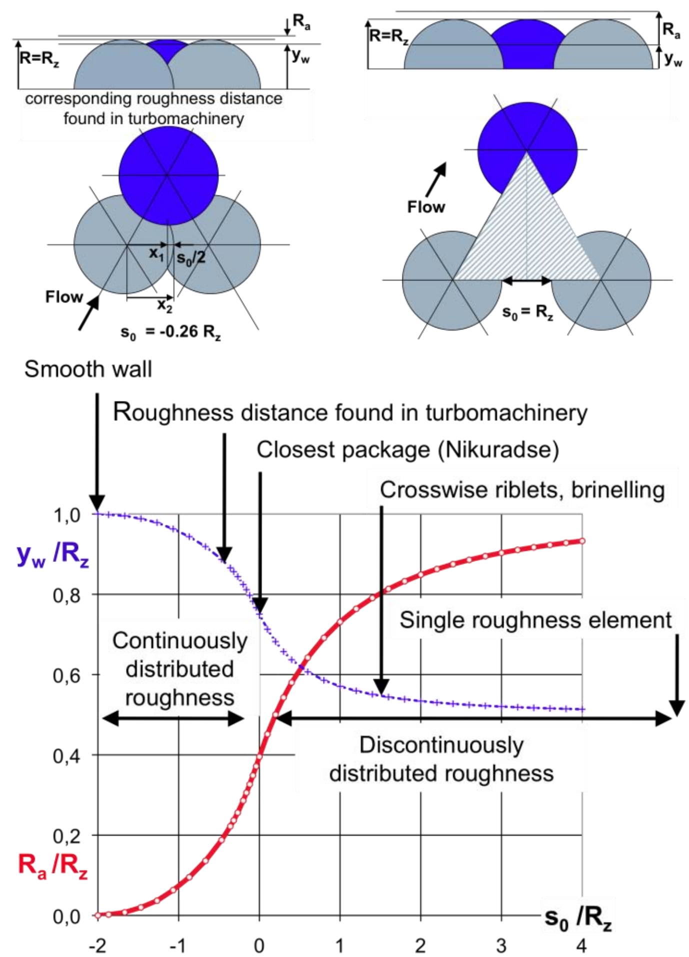

Figure 1: Top: model-roughness of hemispheres with two different distances s_0 between the elements; the centres form an equilateral triangle. **Bottom dotted curve y_w:** the lowering of hemisphere ground zero from wall level with increasing s_0; **solid curve R_a:** averaged roughness above y_w. The ratio R_a/R_z is a unique function of s_0/R_z.

The underlying flow is at first order characterized by the roughness structure parameter s_0/R_z. Moreover, the easy to determine parameter R_a/R_z is a unique function of s_0/R_z. The relation is shown in **Figure 1**.

Because roughness can have different mean distances between the elements, the question of roughness structure is in the same manner relevant for the skin friction of the surface than the height of the roughness element itself.

The distance between the elements classifies three ranges of structures, the continuously distributed range, the range with closest distance between the elements (Nikuradse), and the discontinuously distributed range (see Figure 1).

For the continuously distributed roughness range, the roughness structure parameter varies from the smooth surface with s_0/R_z = -2, over the characteristic roughness found on turbomachinery blades, until small smooth surfaces emerge between the roughness elements for s_0/R_z > -0.26.

Nikuradse‟s measurements have been originally conducted for a certain mean distance between the sand grain roughness elements. Without further prove, he investigated a mean distance near zero between the grains of sand in his famous measurement. So, this range is classified by the closest package distance at $s_0/R_z = 0$.

If there are smooth surface parts between the elements, the roughness is said to be a discontinuously distributed roughness. Here, the roughness structure parameter transitions from the closest package roughness, over the roughness of periodic arranged crosswise obstacles with s_0/R_z = 1 to 2, until for $s_0/R_z \rightarrow \infty$ the condition of a spanwise roughness element is reached.

While continuously distributed roughness found on turbomachinery surfaces is showing only moderate values of k_s/R_z, the roughness structure with s_0/R_z between 1 and 2 can cause dramatic increase of k_s/R_z. The discontinuously distributed roughness is very well suited for high heat transfer rates between the flow and the surface such as heat exchanging devices. However, they should be avoided on turbomachinery surfaces generating high profile losses such as riblets or brinelling arranged perpendicular to the flow.

The correlation k_s/R_z (depending on s_0/R_z) is based on a significant amount of experimental results whereby a series of expense plate experiments on the side-walls of an open oil-channel have been conducted with the same spacing distance between the hemispheres on each plate. Every plate had a different spacing distance. At present, the k_s/R_z correlation is proprietary. For this reason its formulation is not given in this paper.

A deeper understanding can be reached, if the continuously distributed roughness problem is discussed firstly, because fundamental conclusions can be drawn from the observations of the solutions of rough wall modeling. With increasing distance between the roughness elements, the physical situation downstream of each roughness element plays a part and attracts more and more attention. It is believed that the separation behind each element plays the important role for the high loss found for discontinuously distributed roughness in the range s_0/R_z = 1 to 2. Therefore, a significant part of the paper deals with the flow behind the single roughness element. For simplification, the laminar flow in the approaching boundary layer is chosen. Newly undertaken velocity measurements by Montis et al. [7] by hotwire along a low pressure turbine profile suction side and perpendicular to the wall in the “laminar” boundary layer at the location very near the maximal velocity clearly indicate a log layer with respect to mean velocity and a maximum of velocity fluctuations at the lower end of this log layer. This observation in a “laminar” boundary layer was seems unusual. Indeed the length scale found is not high enough and eddy viscosity levels of only $\mu_t/\mu < 20$ are reached. The turbulent energy is still too low for a fully developed turbulent boundary layer.

The single roughness element is selected for investigation. In the spanwise roughness grid study, the gridding is modeled in such a way that all necessary flow features are incorporated. Therefore, calculations with a transition model on a refined inner boundary layer with $y^+ < 1$ and only a modified boundary condition at the wall is used (no modeling by rough wall functions). The calculation results are compared to the experiments of the well-known T106C taken during the UTAT project. Additionally, the progress made during the project is demonstrated on the basis of comparisons at several Reynolds numbers with TATMo's newly measured T106C roughness experiments. The predictions are made using the spanwise gaussian-shape roughness element.

To demonstrate the power of application with wall functions, the CFD result on more industrial configurations is shown at the end.

ROUGHNESS MODELING BY WALL FUNCTIONS

Profiles for velocity

In this section, some of the fundamental concepts introduced by the early investigating pioneers are explored and advanced. For the sake of simplicity, the steady incompressible boundary layer x-component of the momentum equation is considered

$$\bar{u}\frac{\partial \bar{u}}{\partial x} + \bar{v}\frac{\partial \bar{u}}{\partial y} = -\frac{1}{\rho}\frac{\partial \bar{p}}{\partial x} + \frac{1}{\rho}\frac{\partial}{\partial y}\left(\tau + \tau_t\right) \qquad (1)$$

For the inner boundary layer, it is assumed that the left hand side is neglected (convective derivatives). The pressure gradient on the right hand side must be balanced by the shear stress gradients.

Edge of viscous sublayer /log layer: The edge of viscous sublayer /log layer can be defined in different ways. Sometimes it is useful to define this edge when the first deviation from the zero pressure gradient law $u^+ = y^+$ appears (such as the beginning influence of roughness). More often the edge is of interest, where viscous stress and Reynolds stress are equal (change of the exponent of the dissipation per unit turbulent kinetic energy with wall distance from -2 to -1, more in chapter "turbulent kinetic energy and dissipation").

Shear stress velocity: For zero-pressure-gradient, the gradient of shear stress is zero very near the wall. It is common practice to take the shear stress at the wall for the shear stress velocity. However, if the pressure gradient is playing a role it is more useful to take the turbulent shear stress of the viscous log layer (assumed constant in this layer) for deriving accordant coordinates, because only the wall shear gradient is constant in the viscous sublayer, but not the wall shear stress itself. Otherwise u^+_{Wall} becomes infinity and y^+_{Wall} become zero at separation. This situation can be understood in more detail from the comparison in **Figure A1**.

Viscous sublayer: If the turbulent stress is neglected, the viscous sublayer solution, which is the general Couette-flow solution, follows with the boundary conditions at the wall $u(x,0)=0$ and at the edge of the viscous sublayer /log layer $u(x,y_0)=u_o$. In turbulent shear stress wall coordinates the solution is

$$P = -\frac{y_o^{+2}}{2\cdot u_o^+}\cdot P^+$$

$$\frac{u^+}{u_o^+} = \frac{y^+}{y_o^+}\cdot\left[1 + P\cdot\left(1-\frac{y^+}{y_o^+}\right)\right] \qquad P^+ = \frac{\partial \tau^+}{\partial y^+} = \frac{\nu}{\rho\cdot u_\tau^3}\cdot\frac{\partial p}{\partial x} \qquad (2)$$

For zero pressure-gradient and for $u_o^+ = y_o^+$, the well known viscous sublayer solution $u^+ = y^+$ appears.

Viscous log layer: Above the viscous sublayer and in the beginning part of the log layer the laminar shear stress cannot be neglected in comparison to the turbulent shear stress. A solution can be easily found for the zero pressure gradient flow, typically from $30 < y^+ < 300$.

$$u^+ = \frac{1}{\kappa}\cdot\left\{\frac{1}{\eta^+}\left(1-\sqrt{1+\eta^{+2}}\right) + \ln\left|\eta^+ + \sqrt{1+\eta^{+2}}\right|\right\} + C_o$$

$$\eta^+ = 2\cdot\kappa\cdot y^+ \qquad (3)$$

Notice that η^+ is twice Prandtl"s mixing length distance. If $\kappa = 0.40$ is taken for the viscous log layer and $\kappa = 0.38$ (Spalart [17]) for the standard log layer approximation (**Figure 2**) it can be seen that the first solution fits to the measurement-values at low and high y^+ of Nikuradse [2] and to those shown in Hinze [11]. There will be no overshooting of values anymore for the low constant. The otherwise necessary high value of $\kappa = 0.41$ may be avoided by this way. We derived this formulation and found it later in Rotta [12]. However, he defined the origin of η^+ at the edge of viscous sublayer /log layer.

Turbulent log layer: If the laminar shear stress is neglected in comparison to the turbulent shear stress and Prandt"s mixing-length Ansatz is used for the eddy viscosity, the solution is

$\tau_w^+ > 0$:

$$u^+ = \frac{2}{\kappa}\cdot\left\{\sqrt{\tau^+} + \sqrt{\tau_w^+}\cdot\frac{1}{2}\cdot\ln\left|\frac{\sqrt{\tau^+}-\sqrt{\tau_w^+}}{\sqrt{\tau^+}+\sqrt{\tau_w^+}}\right|\right\} + C_1 \qquad P^+\cdot y^+ > 0 \tag{4a}$$

$$u^+ = \frac{2}{\kappa}\cdot\left\{\sqrt{\tau^+} + \sqrt{\tau_w^+}\cdot\frac{1}{2}\cdot\ln\left|\frac{\sqrt{\tau_w^+}-\sqrt{\tau^+}}{\sqrt{\tau_w^+}+\sqrt{\tau^+}}\right|\right\} + C_2 \qquad P^+\cdot y^+ < 0 \tag{4b}$$

$\tau_w^+ < 0$:

$$u^+ = \frac{2}{\kappa}\cdot\left\{\sqrt{\tau^+} + \sqrt{-\tau_w^+}\cdot\arctan\sqrt{\frac{\tau^+}{-\tau_w^+}}\right\} + C_3 \tag{4c}$$

Whereas $\tau^+ = \tau_w^+ + P^+\cdot y^+$ and $\tau_w^+ = 1 - P^+\cdot y_o^+$. The velocity profiles are shown in **Figure 3** for different pressure gradient parameters (top). The massively separated profile with $P = +1.3$ is compared with DNS results (bottom). Notice that the negative velocities of this profile are still also belonging to the log layer range. For zero pressure gradient the well-known law of the wall emerges

$$u^+ = \frac{1}{\kappa}\cdot\ln\left|y^+\right| + u_o^+$$

$$u_o^+ = B - \frac{1}{\kappa}\cdot\ln\left|1.0 + 0.3\cdot k_s^+\right| \tag{5}$$

in which the „constant" u_0^+ is a function of the equivalent sand-grain roughness k_s^+(Schlichting [10] and Nikuradse [3]).

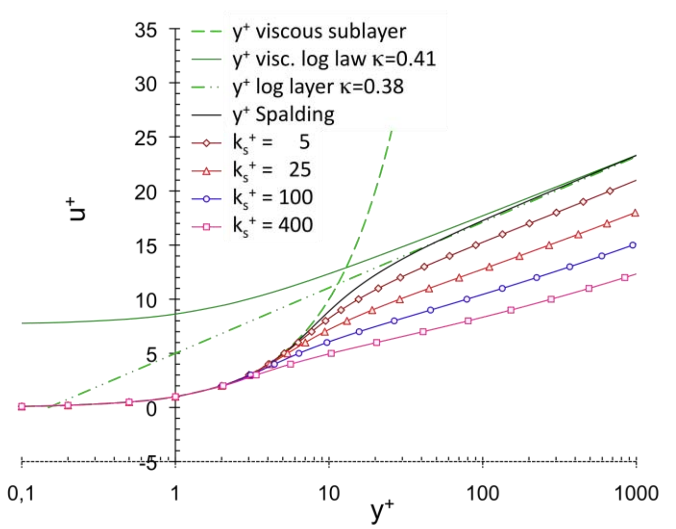

Figure 2: Influence of increasing roughness k_s^+ (from no symbol solid green line to line with squares) on velocity profile of fully developed turbulent boundary layer (in wall coordinates).

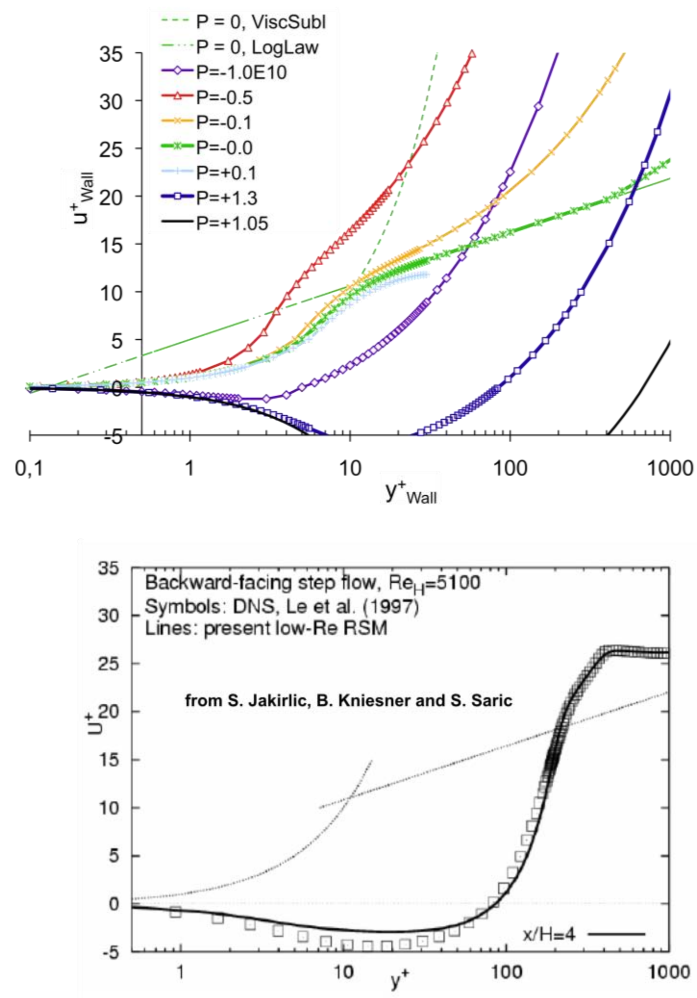

Figure 3: Results of pressure gradient wall function (above) in comparison to RSM and DNS results of Jakirilić [24] (below). Compare the blue squares for P = +1.3 with the black squares for the DNS result.

The ratio k_s^+ and the individually measured surface roughness height R_z depend on the roughness spacing parameter R_a/R_z. This relationship was derived from a model roughness investigation where the spacing between the hemispheres has been systematically varied from negative to positive spacings. Similar results have been found with the procedures of Waigh and Kind [5] and Rij et al. [6]. Montis et al. [7] documented this for the investigations of two cascade designs with different pressure distribution. An important contribution on the influence of different rough surface structures is also given in Acharya et al. [4].

Overall approximation: A common approximation both of the solution for the viscous sublayer and of the turbulent log layer can be constructed with the help of perturbation methods, where after Spalding [13] only the sum of the first 4 terms is kept of the Taylor series of the exponential function from the inverse log law.

$$y^{+} = u^{+} + e^{-\kappa \cdot u_o^{+}} \cdot \left[e^{\kappa \cdot u^{+}} - 1 - \kappa \cdot u^{+} - \frac{\left(\kappa \cdot u^{+}\right)^2}{2} - \frac{\left(\kappa \cdot u^{+}\right)^3}{6} - \frac{\left(\kappa \cdot u^{+}\right)^4}{24} \right] \tag{6}$$

Profiles for turbulent variables

Turbulent kinetic energy and dissipation: If the solutions of the two-equation models are approaching $y^{+} \to 0$ then the viscous sublayer solutions will appear, Wilcox [14]:

$$k = k_{\log Law} \cdot \left(y^{+}/y_o^{+}\right)^{3.31} \qquad \omega = \frac{u_\tau^2}{\nu} \cdot \frac{6}{\beta} \cdot \left(y^{+}\right)^{-2}, \qquad \text{Smooth} \tag{7a}$$

$$\omega = \frac{\omega_{wall} = u_\tau^2/\nu \cdot S_R}{\left(1 + \sqrt{S_R \cdot 6/\beta} \cdot y^{+}\right)^2}, \qquad \text{Rough} \tag{7b}$$

And as $y^{+} \to \infty$ (Edge of log layer /outer layer) the solutions for the log layer are:

$$k = k_{\log Law} = u_\tau^2 / \sqrt{\beta^*} \qquad \omega = \frac{u_\tau^2}{\nu} \cdot \frac{1}{\sqrt{\beta^*} \cdot \kappa} \cdot \left(y^{+}\right)^{-1} \tag{8}$$

If these solutions are taken in each case for $F(y^{+})_{ViscSub}$ and $F(y^{+})_{LogLaw}$, then the following weighting function will give the right behavior from the value at the wall until the end of the log layer, **Figure 4**.

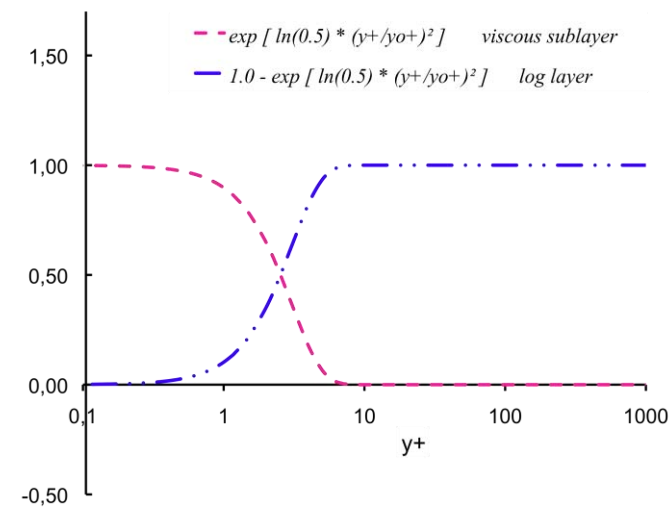

Figure 4: Weighting function for common viscous sublayer and log layer solution for $k_s^{+} = 10$.

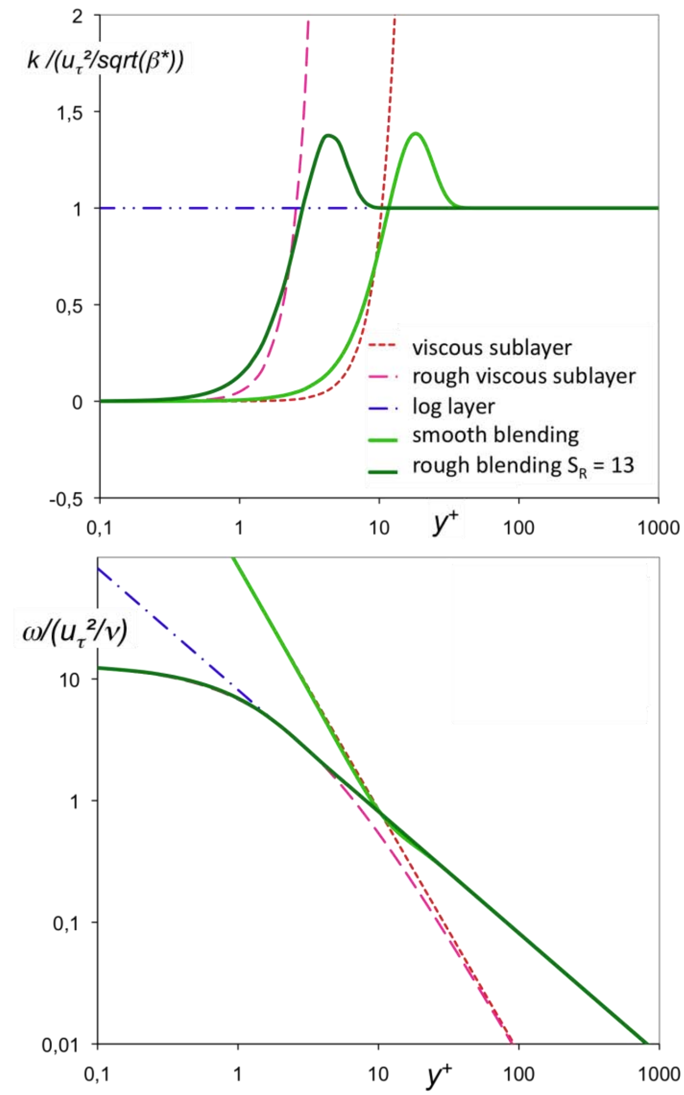

Figure 5: The k and ω weighting function for smooth $k_s^{+} < 5$ and transitional-rough wall at $k_s^{+} = 10$.

$$F(y^{+}) = e^{\left[\ln(0.5)\cdot(y^{+}/y_o^{+})^2\right]} \cdot F(y^{+})_{viscSub} + \left[1 - e^{\left[\ln(0.5)\cdot(y^{+}/y_o^{+})^2\right]}\right] \cdot F(y^{+})_{\log Lay} \tag{9}$$

Applied for k and ω the result is shown in **Figure 5**. Compare the transition of the two proposed functions (green) from the smooth and the rough viscous sublayer solution (red) to the common (subjacent) log layer solution (blue). The light green is for the smooth wall and the dark green is for the rough wall.

The overshoot of turbulent kinetic energy, typically not found in wall function simulations with the k-◆ model, is artificially modeled by the effect of the weighting function.

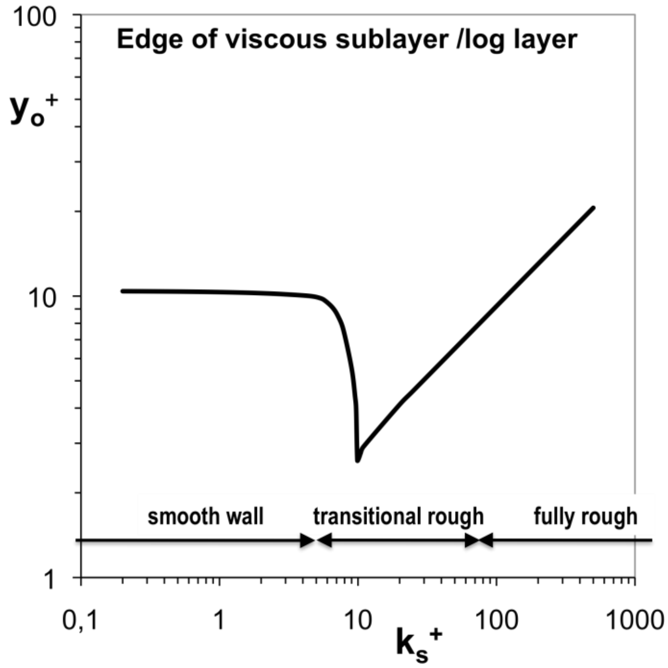

Figure 6: Variation of y_0^+ edge of viscous sublayer /log layer with equivalent sand grain roughness. Compare the similar course of curve with the Spalart-Allmaras turbulence model in Durbin et al [16].

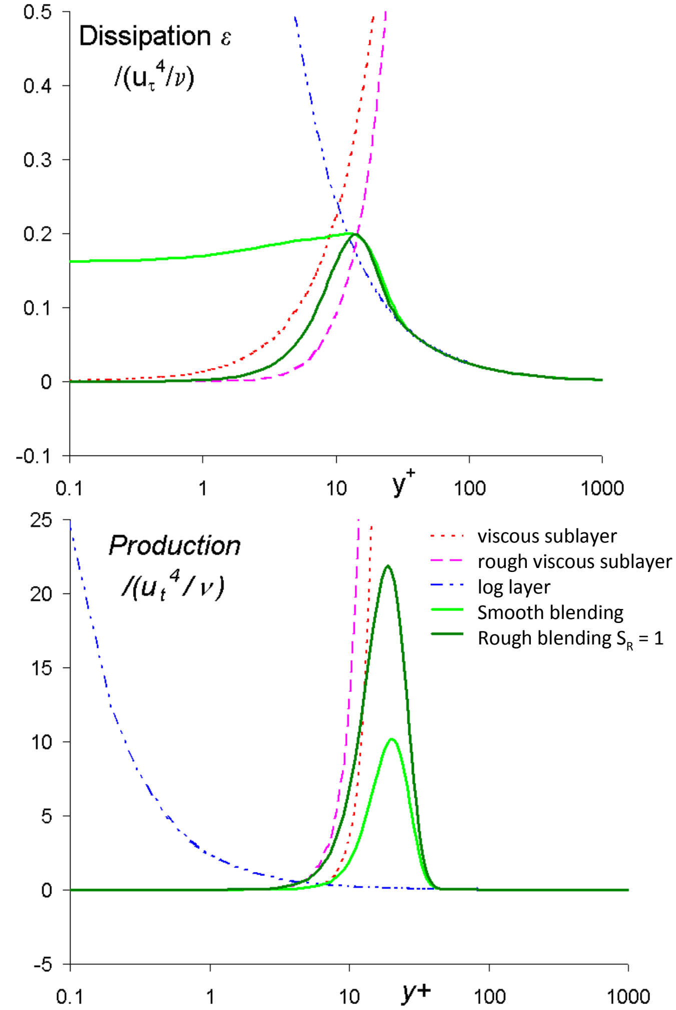

Figure 7: Losing its dissipation of turbulent kinetic energy in the viscous sublayer and Rising the production near the edge viscous sublayer /log layer for the rough wall with k_s^+ = 100 (notice the different scaling on the Y-axis).

This overshoot is evident in the Channel-flow results (DNS data) shown in Durbin and Petterson-Reif [15]. With increasing roughness the dissipation per unit turbulent kinetic energy is lowered at the wall. As a consequence, the -1 exponent behavior of the log layer is apparently extended nearer to the wall for S_R = 13 or k_s^+ = 10. The edge of viscous sublayer /log layer has reduced from y_0^+ = 10 to the minimum near y_0^+ = 2.6, **Figure 6**. From the minimum on, the edge of viscous sublayer /log layer is again departing from the wall with an exponent of +0.5 for the entire fully rough regime.

Modifications for production of boundary fluxes: Considering the changed fluxes for the first wall cell, modifications for the right hand side on both equations of the turbulence model are applied. An excess of production of turbulent kinetic energy in comparison to the smooth surface is apparent.

For a rough wall with k_s^+ = 100 it can be seen from **Figure 7** that the viscous sublayer has lost nearly all its potential of dissipation the turbulent kinetic energy in the viscous sublayer. On the other hand an excess of production of turbulent kinetic energy near the edge of viscous sublayer /log layer is apparent in comparison to the smooth wall.

Overall it must be concluded that the main effect of the fully rough wall is the increase of turbulent kinetic energy in the inner boundary layer.

NUMERICAL METHOD

TRACE is the CFD solver for internal flows at the German Aerospace Center (DLR). It is a three-dimensional, steady and unsteady flow solver for the Favre- & Reynolds-averaged compressible Navier-Stokes equations. TRACE is focused on the CFD of turbomachinery, therefore it is integrated in the design process of the MTU Aero Engine GmbH. It has a wide variety of models adapted especially to turbomachinery flow, e.g.: two equation turbulence model based on Wilcox k-ω model, multimode transition model [22] and alternatively the γ - $Re\theta$ transition model according to Menter [21]. All included models are at least second order accurate in space and time. For more details, please refer to the references [18] and [19]. In the calculations of continuously distributed roughness, wall-functions have been used, and in the calculations with the spanwise roughness element one of the transition models has been selected. The inner layer has been resolved with a grid cell center distance from the wall of $y^+ < 1$.

RESULTS AND DISCUSSION

The flow on turbomachinery blade surface, which is provided with roughness element along the span, cannot be calculated with standard state-of-the-art calculations, because standard grid generation does not allow the necessary resolution for the flow around the obstacle. The flow however needs such a high resolution, because it is drastically altering around the roughness element with immanent steep velocity gradients in stream-wise and in surface-normal directions and for some 3d-roughness element also in spanwise direction.

One possible solution is to use a model for the spanwise roughness. The model should give all the sources necessary to account for the effect in the equations. Marciniak [25], Pacciani [26] and de Saint Victor et al. [27] have proceeded in this direction.

Refinement of roughness element

The other way is the refinement around the element, where parts of the standard grid are removed from the 1:1 connectivity between the block parts. The removed parts are refined or replaced with an adequate resolution and are again appended to form a modified connectivity at the panel surfaces of the blocks. The panel surfaces with unequal connectivity are treated by a special approach called “zonal” interface [20]. In the following, most of the validations have been done with this approach.

The TATMo experiments were carried out with a circular wire along the span. Originally planned was a roughness element with a “Gaussian” shape. Séraudie [28] however found out that the roughness height is the determinant parameter for loss, and that there is no effect of the roughness shape at first order. With this observation, TATMo‟s roughness experiments have been performed with a spanwise roughness element of a circular wire, Michalek [30]. Most of the comparing calculations have been validated by these measurements.

Influence of roughness step location and step length

Figure 8 is showing the refined grid blocks around the roughness element located at 60% and 66,4% axial chord for the study of influence on loss at different element positions. Fully turbulent and transitional (Multimode) results at midspan are compared in **Figure 9** to UTAT measurements during the early validation work with the smooth (left hand) and the “full step” at 66% (to the right).

The comparison in **Figure 10** depicts the same deep but less wide wake at 120.000 for the smooth surface and less deep but wider wake for the rough surface.

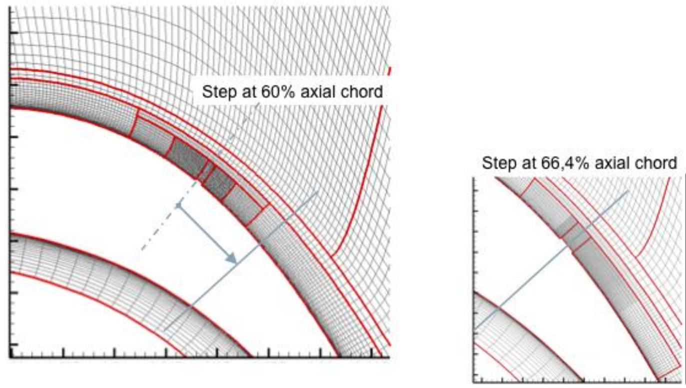

Figure 8: Variation of roughness location. Individually refined grid around roughness element in spanwise and in streamwise direction for both locations.

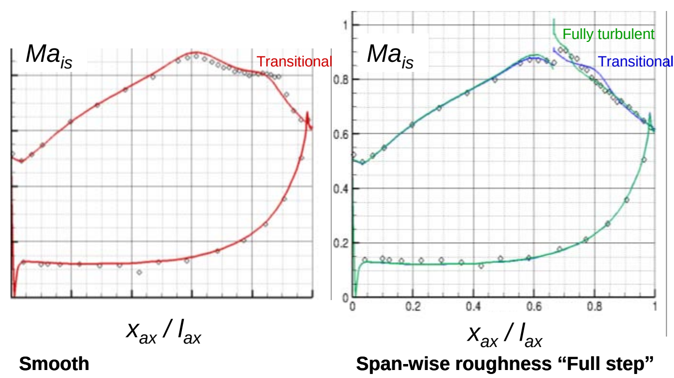

Figure 9: Comparison of Mach-number distribution at mid-span for smooth and refined spanwise roughness element “Full step” at Re=120.000, UTAT measurements.

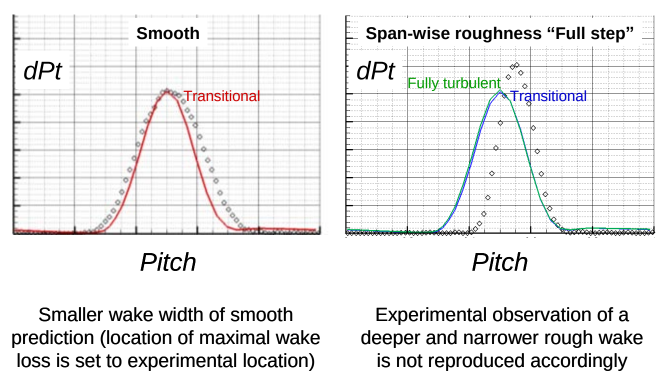

Figure 10: Comparison of wake profile downstream in blade row direction with the UTAT experiment.

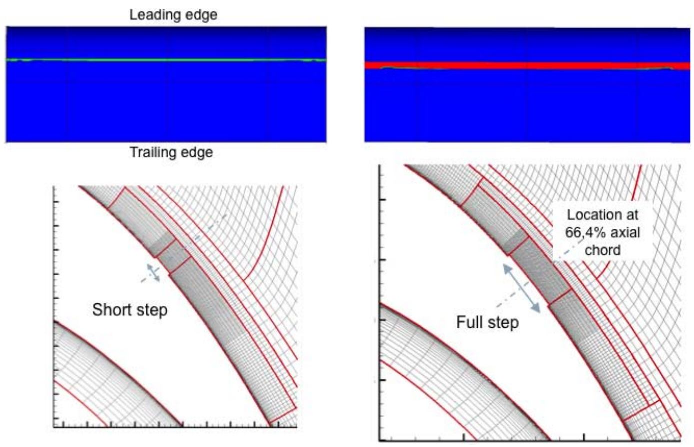

Figure 11: Variation of step length.

The difference between smooth and rough is hardly seen between the calculation results, reflecting nearly same loss at this Reynolds-number. In the same way the influence of the length of the step has been studied, **Figure 11**. The results reveal a very small influence of step length on loss at midspan (not shown).

Spanwise roughness element "Wavy step"

Additionally, the 3d-roughness element ("Wavy step", **Figure 12**) was modeled and compared with the short and long step results.

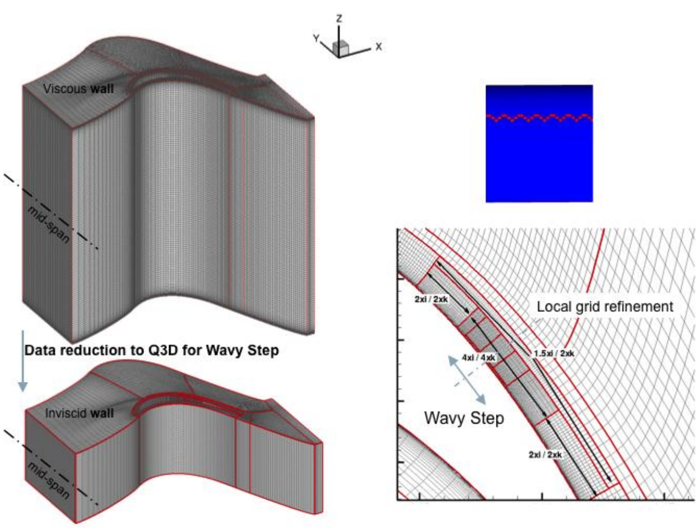

Figure 12: Representation of the "Wavy step" (top to the right): the need of local grid refinement and data reduction to account for spanwise roughness element "Wavy step".

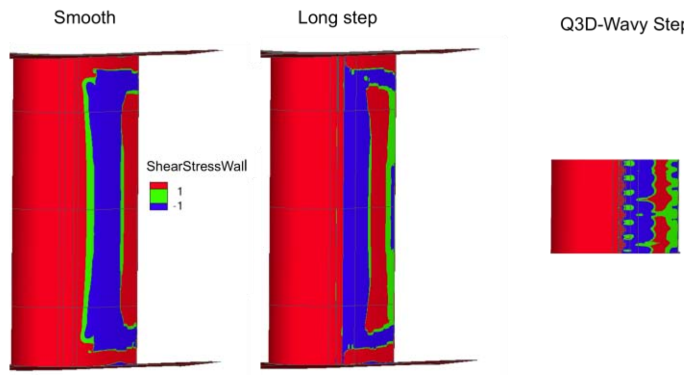

Figure 13: Comparison of wall shear stress for smooth, "Full-step" and "Wavy-step" on the suction surface.

The "Wavy step" has been experimentally investigated during the predecessor project UTAT. To reduce the amount of grid points for this 3-roughness element, a smaller grid block has been cut out from the full 3d-model.

Only the remaining block has been calculated. At both cut surfaces the slip boundary condition (in-viscid wall) has been applied.

The shear-stress-results on the suction side of **Figure 13** document the shortening of the separation length by the "Full-step" roughness element (in the middle) compared to the results of the smooth surface (on the left). The development along the span and the additional variation in spanwise direction for the "Wavy step" can be read out from the Q3D results on the right. On average, the reduction of separation length of "Wavy step" and "Full-step" is the same.

2D-Gauss element and 2D-Rectangular Groove

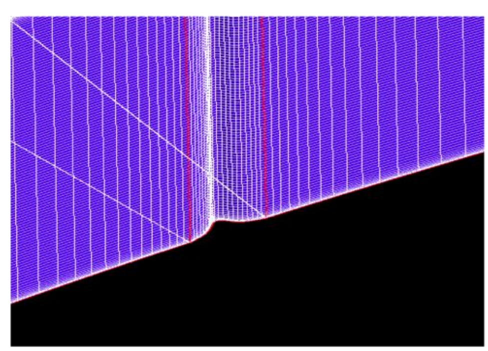

Spanwise roughness location x_{ax}/l_{ax} = 66.4%
length = 0.8 mm

Rectangular /Gaussian: height = 0.2 mm
Groove: depth = 0.2 mm

Figure 14: Gaussian shape element

Comparison of multimode- and lapse-rate figure

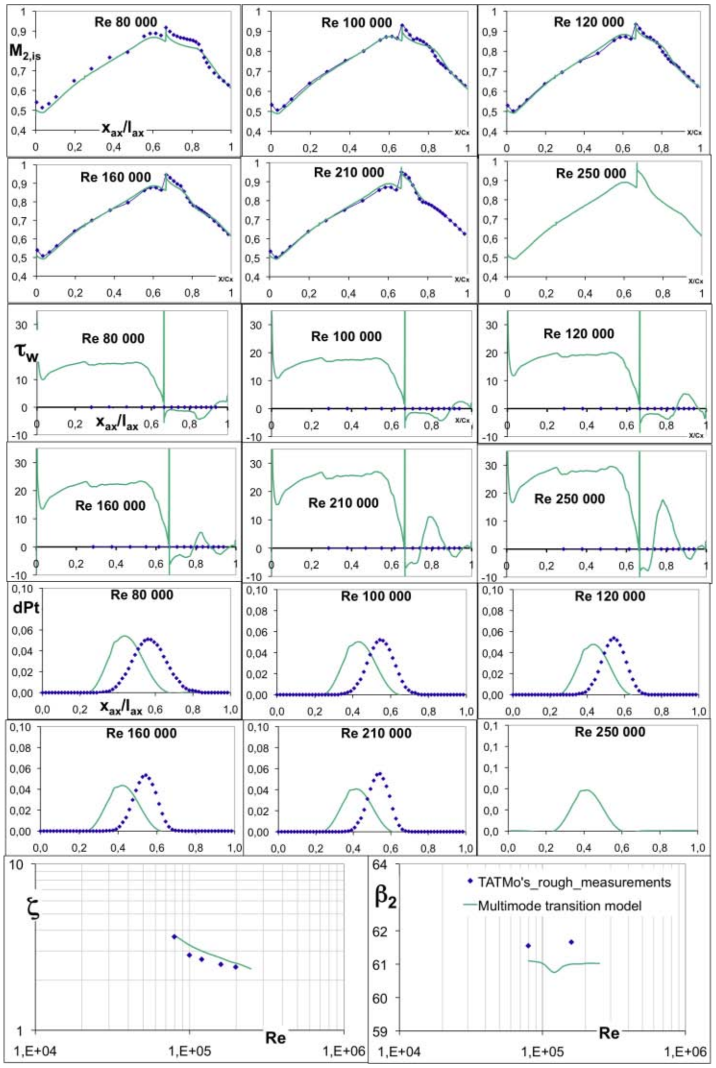

Figure 15: Comparison of multimode- and γ-Reθ transition model calculations with experiment for T106C-rough results, partner result workbook distributed by de Jaeghere [31].

Since nearly the same loss was calculated for all roughness elements with identical step height including the “Wavy step”, all subsequent simulations for the validation work with the TATMo experiment have been performed with the 2D-Gauss element, **Figure 14**. Before that, it was tried to follow the different results given in the measurements by Himmel [29], to find the same behavior in the predictions. These reproduce the same tendency: Most low loss for the 2D-Rectangular Groove vs. the Smooth surface at lower Reynolds numbers and highest loss for the 2D-Rectangular step vs. the 2D-Gauss element at the highest Reynolds-number (result not shown).

Comparison of “lapse-rate” results

While the results with the Multimode transition model in **Figure 15** excellently matches the measured Mach-number distributions particularly around the roughness element located at $x/l_{ax} = 0.66$, the results with the γ - $Re\theta$ transition model still show no roughness element based reduction of separation length for all Reynolds-numbers (not shown).

From the calculated wall shear stress distributions it is seen that “Multimode” (green) is calculating a second small separation bubble near the trailing edge of the profile for all Reynolds-numbers above 100.000, whereas no such situation appears for the flow below 100.000. The second separation bubble may be attributed to a turbulent separation with turbulent reattachment downstream the transitional separation bubble due to the more thickened boundary layer following the roughness element. For the flow below 100.000, the massive separation documented for the smooth wall in Fiala [9] is reduced to a still large separation bubble but well attaching before the trailing edge as a consequence of the spanwise roughness element.

The result with the γ-Reθ transition model seems to be completely insensitive to the roughness element. The model has to be improved in this regard for the future. The comparison of the wake profiles displays a systematic offset between measurement and calculation results.

For the Multimode transition model the integral loss at all Reynolds-numbers is excellently reflected. The wake-profiles do match sufficiently for the low Reynolds-numbers. Still, they are for the high numbers somewhat deeper and less wide at same integral value. This differs from the comparisons made during the early validation phase (UTAT measurements), and no explanation has been found yet. Two differences are worth mentioning: Firstly, the traversing location of the TATMo measurement is somewhat downstream of the blade trailing edge (43,6 mm) in comparison to (37,1 mm) of the UTAT measurement. Secondly, the separation length of the TATMo experiment is longer than the of the UTAT experiment.

The comparison of the integral-exit angles displays slightly more turning for the Multimode results.

CFD application on more industrial configurations

Finally the numerical computation with improved wall-function modeling has been performed on more industrial configurations, such as on a one-stage compressor and on an 8-stage compressor. The first example shows the influence of the consideration of pressure gradient in the law of the wall only and the second example reveals the additional influence of roughness on efficiency in calculations using the modified wall-functions.

The comparison results of calculations with both the standard wall-functions on all surfaces and the modified wall-functions are shown in **Figure 16** for the one-stage research compressor. The improved wall-functions consider the pressure gradient for the identification of shear stress velocity. While at the Aerodynamic Design Point (ADP) operation condition almost no difference in pressure distribution and wall shear stress do occur, the differences appear clearly in the results at an operating condition near stall (exit pressure was 13% higher than at ADP).

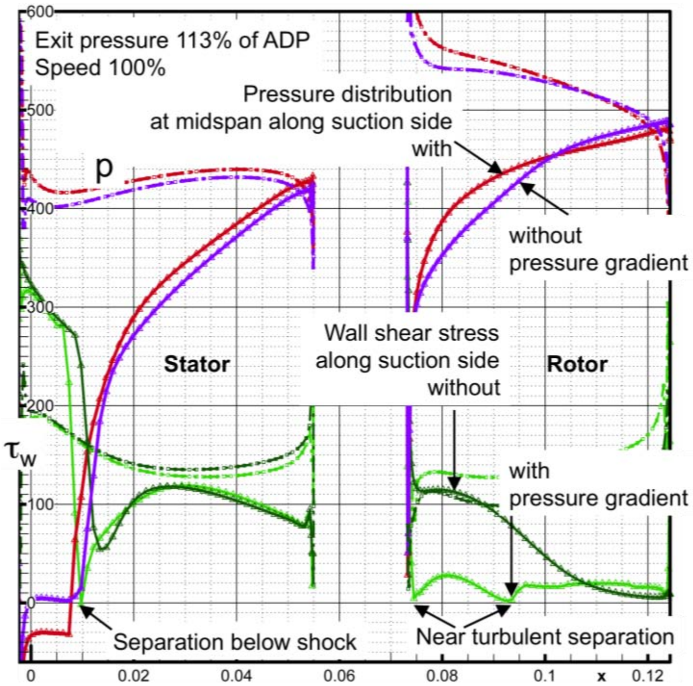

Figure 16: Comparison of calculations with and without consideration of pressure gradient in the law of the wall. More low wall shear stress (light green relative to dark green) at the suction side of the rotor blade reveals a closer to stall-condition for the calculation with wall-functions accounting for pressure gradient.

The numerical computation result with wall-function roughness modeling of the 8-stage compressor (**Figure 17**) is displaying an overall loss of 2% in efficiency for k_s = 10 µm at all blades. Passing wakes have been considered with the Quasi-unsteady transition modeling after the approach of Kozulovic et al. [23]. With increasing roughness more time-steps have been needed for the same status of convergence. The same drop in efficiency has been experimentally proved for a five-stage high-pressure compressor with excessive roughness at the rotor surfaces, documented by Schäffler [8]. The validation result shown in previous chapter was enriched by the experience produced during this application work. In particular the significant influence of roughness on compressor's stage matching is highlighted for transonic flows.

CONCLUSIONS AND ANALYSIS

Surface roughness can have a profound effect on losses and on heat transfer. Surfaces on turbomachinery blades often show distributed roughness. The roughness stems from machining processes, from manufacturing imperfections, and the blades are subjected to erosion by impinging of particles from the combustion process in the course of their lifetimes.

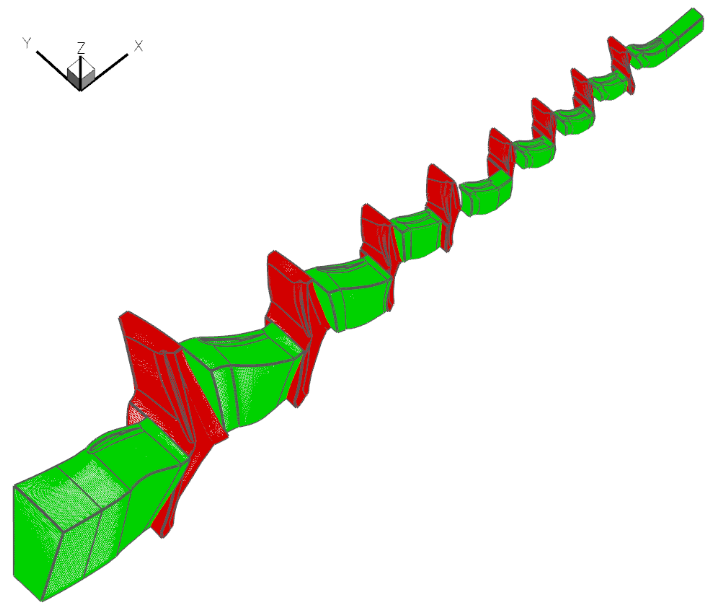

Figure 17: CFD application of roughness modeling

The layer very near the surface, the viscous sublayer, looses its ability for dissipation of turbulent motions. In parallel, the height of this layer is lowered for the intermediate or transitional-rough wall. For further increased roughness, for fully rough walls, the height of the sublayer again recovers but at the expense of increased production of turbulent motions. It becomes clear that momentum exchange and that heat transfer rates are dramatically affected by this.

This enhanced momentum exchange plays also the important role for the spanwise roughness element. However, the effect is mainly locally restricted to the region downstream the roughness element to increase the amplification of disturbances in the approaching laminar boundary layer or at least to introduce significant disturbances for a High-lift rear loaded design of a Low Pressure Turbine. This helps a separation bubble to reattach well before the trailing edge, so that no minder-deviation of the blade"s flow angle occurs.

The reduction of separation length is clearly seen experimentally and can be very well reproduced by the calculations with the multimode transition model. For this model, the integral-loss at all Reynolds-numbers are excellently reflected. The wake-profiles do match sufficiently for the low Reynolds-numbers.

However, beside the correct reproduction of flow quantities for the spanwise roughness element, the right assessment of distributed roughness on surfaces of an industrial configuration is important. Because a high grid resolution very near the wall on all surfaces is not always possible, the problem can be solved with the help of wall-functions. The results of the applications document the significance of rough wall-function modeling for turbomachinery.

ACKNOWLEDGMENTS

The research reported in this paper was undertaken within the research project TATMo funded (contract No. AST5-CT-2006-030939, www.tatmo.eu) by the European Commission. We thank our fellow partners in European Union FP6 programme TATMo for permitting the publication of our results in this paper. Additionally the authors want to thank Florian Herbst for his support and experience with the local grid refinement. The authors are also grateful to all anonymous reviewers for their comments that led to various improvements of the paper.

NOMENCLATURE

β_2	exit angle
$\beta, \beta*$	constants in dissipation terms of k-w model
DNS	Direct Numerical Simulation
dPt	$(P_{01}-P_{02})/P_{01}$
η	twice Prandtl"s mixing length distance
k, tke	turbulent kinetic energy (m^2/s^2)
k_s	equivalent sand grain roughness (μm)
κ	first constant in logarithmic law of the wall
l_{ax}	axial blade length at midspan (m)
$M_{2,is}$	isentropic Mach number
μ_t	eddy viscosity (kg/ms)
ν	kinematic viscosity (m^2/s)
ω	dissipation per unit tke (1/s)
p	pressure (Pa)
P	pressure gradient parameter
ρ	density (kg/m^3)
Re	chord Reynolds number
$Re\theta$	Momentum thickness Reynolds number
R_a	averaged roughness above y_w (μm)
R_z	characteristic roughness element height (μm)
s_0	distance between hemispheres at ground zero
S_R	dimensionless surface roughness function
τ	shear stress (Pa)
TATMo	Turbulence And Transition Modellling, EC-Project
UTAT	Unsteady transitional flows in Axial Turbomachines
u, v, w	velocity components (m/s)
u_t	shear stress velocity (m/s)
u^+	mean velocity in wall coordinates
x, y, z	cartesian coordinates (m)
x_{ax}	axial distance from the leading edge (m)
y_w	distance above hemisphere ground zero
y^+	characteristic wall distance
ζ	$1-\frac{1-(P_2/P_{02})^{(\gamma-1)/\gamma}}{1-(P_2/P_{01})^{(\gamma-1)/\gamma}}$ kinetic loss of cascade at midspan

Superscripts

+	based on characteristic shear stress velocity
–	time averaged quantity
~	pitchwise mass-flow averaged value

Subscripts

0	indicative for edge of viscous sublayer /log layer
1	inlet
2	exit
ax	in axial direction
w	value at the wall

REFERENCES

[1] Bons, J. P., 2010, „A Review of Surface Roughness Effects in Gas Turbines“, *Journal of Turbomachinery*, Vol. 132 / 021004-1, April 2010.

[2] Nikuradse, J., 1932, „Gesetzmäßigkeiten in glatten Rohren“, Forschungsheft 356, VDI-Verlag GmbH / Berlin NW7.

[3] Nikuradse, J., 1933, „Strömungsgesetze in rauen Rohren“, Forschungsheft 361, VDI-Verlag GmbH / Berlin NW7.

[4] Acharya M., Bornstein J., Escudier M. P., 1986, "Turbulent boundary layers on rough surfaces", *Experiments in Fluids* 4, 33-47, Springer-Verlag.

[5] Waigh, D. R., and Kind, R. J., 1998, “Improved Aerodynamic Characterization of Regular Three Dimensional Roughness”, AIAA Journal, 36, pp. 1117-1119.

[6] Rij J. A., Belnap B. J., Ligrani P. M., 2002, "Analysis and Experiments on Three-Dimensional, Irregular Surface Roughness", *Journal of Fluids Engineering*, Vol. 124, pp. 671 - 677.

[7] Montis M., Niehuis R., Fiala A., 2011, "Aerodynamic Measurements on a Low Pressure Turbine Cascade with Different Levels of Distributed Roughness”, ASME Paper GT2011-45015.

[8] Schäffler, A., 1979, “Experimental and Analytical Investigation of the Effects of Reynolds Number and Blade Surface Roughness on Multistage Axial Flow Compressors”, ASME Paper No. 79-GT-2.

[9] Fiala, A., 2009, “Report on CFD on separation bubble in turbine applications”, TATMo-Report-D3A.1.1.2-MTU-V02.

[10] Schlichting, H., 1982, “Grenzschicht-Theorie”, 8. Auflage, Verlag G. Braun Karlsruhe.

[11] Hinze, J. O., 1987, “Turbulence“, 2nd Edition, Figure 7-9, p. 627, ISBN 0-07-029037-7.

[12] Rotta, J., 1950, „Das in Wandnähe gültige Geschwindigkeitsgesetz turbulenter Strömungen“, Ingenieur-Archiv, XVIII, 277-280, Max-Planck-Institut für Strömungsforschung Göttingen.

[13] Spalding, D. B., „A Single Formula for the Law of the Wall“, ASME, *Journal of Applied Mechanics*, p. 455-458, September 1961.

[14] Wilcox, D. C., 2006, “Turbulence Modeling for CFD”, 3rd edition, DCW Industries Inc., La Cañada, CA, USA, ISBN 978-1-928729-08-2.

[15] Durbin, P. A., and Petterson-Reif, B. A., 2001, “Statistical Theory and Modeling for Turbulent Flows”, Wiley, ISBN 0471 297444, Figure 6.55, page 113.

[16] Durbin P. A., Medic G., Seo J.M., Eaton J. K., Song S., 2001, “Rough Wall Modification of Two-Layer k-ε”, *Transactions of the ASME*, Vol. 123, March.

[17] Spalart, P. R., 2009, “The Law of the Wall, Indications from DNS, and Opinion”, Workshop on Progress in Wall Turbulence: Understanding and modeling, Lille (France): April 21-23.

[18] Franke M., Kügeler, E., and Nürnberger, D., 2005, “Das DLR Verfahren TRACE: Moderne Simulationstechniken für Turbomaschinenströmungen”, in: Proc. Deutscher Luft- und Raumfahrtkongress 2005, Friedrichshafen, Germany, Paper DGLR-2005-211.

[19] E. Kügeler, D. Nürnberger, A. Weber, and K. Engel, Influence of blade fillets on the performance of a 15 stage gas turbine compressor. *ASME Turbo Expo*. GT2008-50748 (2008).

[20] Yang, H., Nürnberger, D., Kersken, H.-P.: “Toward Excellence in Turbomachinery Computational Fluid Dynamics, 2006, “A Hybrid Structured-Unstructured Reynolds-Averaged Navier-Stokes Solver”, ASME Transactions, Journal of Turbomachinery, pp. 390-402, Vol. 128, 2006.

[21] Langtry, R. B., Menter, F. R., Correlation-Based Modeling for Unstructured Parallelized Computational Fluid Dynamics Codes, AIAA Journal 47-12, 2894-2906 (December 2009).

[22] Kožulović D., Röber T., Nürnberger D., 2007, „„Application of a Multimode Transition Model to Turbo machinery Flows““, Proc. 7th European Turbomachinery Conference, Athens, Greece, March 2007.

[23] Kožulović, D., and Röber, T., 2006, ”Quasi-Unsteady Transition Modelling of Periodic Wakes”, Turbulence, Heat and Mass Transfer 5, K. Hanjalić, Y. Nagano and S. Jakirilić (Editors).

[24] Jakirilić S., 2010, “Turbulente Scherströmungen, Turbulenz”, Physik der Turbulenz und Turbulenzmodellierung, 1. -4., März, 2010, Erlangen.

[25] Marciniak, V., 2008, “Report on Validation of the Models for Separation Bubbles”, TATMo-Report-D3A.1.1.3-DLR-V1.0, May 26.

[26] Pacciani, R., and Marconcini, M., 2009, “Report on Models for spanwise Roughness”, TATMo-Report-D3A.2.1.2-UNIFLO-V1.0, Apr 10.

[27] de Saint Victor, X., and Billonnet, G., 2010, “Report on Validation of the Models for Spanwise Roughness”, Report TATMo-R-D3A.2.1.3-ONERA/V01, March.

[28] Séraudie, A., and Dor, J., 2008, “Fundamental Investigation on spanwise roughness”, TATMo-Report-D2A.1.3-ONERA-V1.0, Sep. 3.

[29] Himmel, C., and Hodson, H., 2008, “The Choice of Passive Flow Control Devices”, TATMo-Report-D2A.2.4.4-UCAM-V4.0, Dec. 10.

[30] Michalek, J., and Arts, T., 2008, “Steady state performance of the T106C blade. Free-stream turbulence and bursting analysis”, TATMo-Report-D2A.2.1.4-VKI-V01, October 30.

[31] de Jaeghere, E., 2009, “Workbook of partners with comparisons of roughness results of T106C with spanwise 2D-Cylindrical wire attached to the surface”, TATMo-Snecma.

ANNEX A: SHEAR STRESS COORDINATES

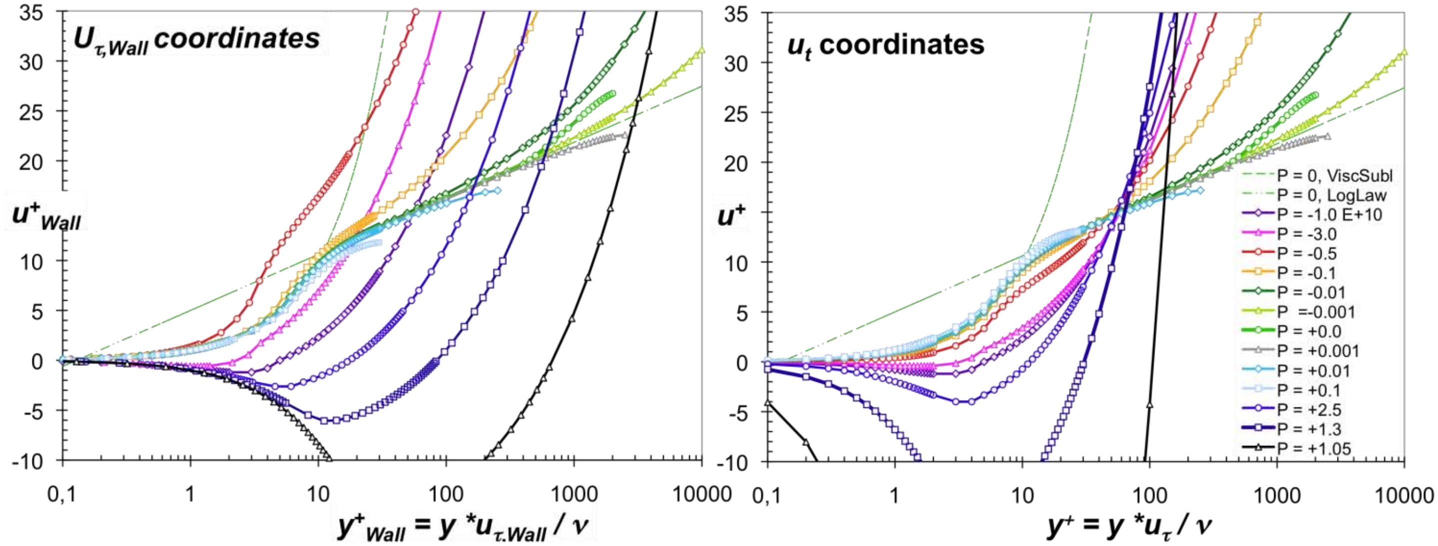

Figure A1: Separated velocity profile *P* = -1.0 for separation not seen in wall-shear coordinates but in log layer-shear coordinates. Massive separation identified by *P* > 1 and negative velocities in the log layer.